Tailoring Renal Clearable Zwitterionic Cyclodextrin for Colorectal Cancer-Selective Drug Delivery

Min-Jun Baek
College of Pharmacy and Research Institute of Pharmaceutical Sciences, Seoul National University
Duy-Thuc Nguyen
College of Pharmacy and Research Institute of Pharmaceutical Sciences, Seoul National University
Dahan Kim
College of Pharmacy and Research Institute of Pharmaceutical Sciences, Seoul National University
So-Yeol Yoo
College of Pharmacy, Chungnam National University
Sang Min Lee
College of Pharmacy, Chungnam National University
Jae-Young Lee
College of Pharmacy, Chungnam National University
Dae-Duk Kim (ddkim@snu.ac.kr)
College of Pharmacy and Research Institute of Pharmaceutical Sciences, Seoul National University
https://orcid.org/0000-0003-0093-3874

Article

Keywords: cyclodextrin, renal clearable, zwitterionic, off-target accumulation, colorectal cancer

Posted Date: November 8th, 2022

DOI: https://doi.org/10.21203/rs.3.rs-2200358/v1

Version of Record: A version of this preprint was published at Nature Nanotechnology on April 27th, 2023.
See the published version at https://doi.org/10.1038/s41565-023-01381-8.

Abstract

Although cyclodextrin (CD)-based renal-clearable nanocarriers have a high potential for clinical translation in targeted cancer therapy, their optimal designs for enhanced tumor retention and reduced off-target accumulation have rarely been proposed. Herein, we present a delicately tailored structure of a renal-clearable zwitterionic CD, hepatkis-(6-deoxy-6-((phenylboronic acid-tetraethyleneglycol-l-glutamic acid N^{α}-sulfobetaine)-octaethyleneglycol-caproamide))-β-cyclodextrin (PBA-(ZW)-CD), for colorectal cancer (CRC)-selective drug delivery. Twenty CD derivatives with different charged moieties and spacers are synthesized and screened for colloidal stability. The resulting five candidates are complexed with adamantyl sulfocyanine 7 and evaluated for biodistribution. PBA-(ZW)-CD, the optimized structure, displays a high tumor-to-background ratio of 3.7–4.1. PBA-(ZW)-CD inclusion complexes of doxorubicin and ulixertinib are fabricated, and their enhanced tumor accumulation (vs. free doxorubicin, 2.0-folds; vs. free ulixertinib, 2.1-folds), facilitated elimination (vs. free doxorubicin, 15.2 and 0.0% remaining in the heart and muscles, respectively; vs. free ulixertinib, 17.7 and 7.4% in the liver and kidneys, respectively), and tumor penetration comparable to those of free drugs are verified *via* mass-spectrometric quantitation and imaging. The improved antitumor efficacy of PBA-(ZW)-CD/drug combination therapy is demonstrated in heterotopic and orthotopic CRC models (vs. free drug combination, tumor size reduction by 52.0 and 76.2%, respectively), suggesting that PBA-(ZW)-CD can be used as a promising CRC-targeted nanoplatform.

1. Introduction

Despite the remarkable progress in nanotechnology and biomedical engineering, only a few injectable medical nanocarriers (NCs) are currently available for cancer diagnosis and treatment. This is mainly due to potential toxicity concerns caused by off-target accumulation and long-term retention of NCs in normal organs[1,2,3,4,5,6]. Uncontrolled distribution profiles may result from the non-renal-clearable particle size (> 10 nm), which is a primary prerequisite of conventional NCs utilizing the enhanced permeability and retention (EPR) effect[1,2,5,6,7]. With a limited clinical translation rate, this old-school NC design faced a paradigm shift towards a renal-clearable ultrasmall nanoplatform[8,9,10,11,12,13,14,15], which has several advantages compared to its non-renal-clearable counterpart: (1) rapid elimination of NCs distributed to off-target tissues *via* urinary excretion, (2) high tumor vascular permeability, and (3) highly reduced uptake by the mononuclear phagocyte system (MPS)[9,16,17]. These favorable features allow the high-dose administration of cytotoxic cargo molecules with increased tumor selectivity, resulting in enhanced efficacy and minimal adverse effects[9,16,18,19,20,21,22].

However, renal-clearable NCs are not free from drawbacks that hamper their clinical translation. One major drawback is the residual toxicity caused by trace amounts of injected NCs, which may face inadvertent chronic accumulation[23,24]. Notwithstanding the short-term biocompatibility, long-term or lifetime exposure to undegradable foreign materials, such as silica, metal, and synthetic polymer nanoparticles, discourages their clinical use[25,26]. To address this issue, renal-clearable NCs, namely H-

Dots, composed of biodegradable organic materials including β-cyclodextrin (CD)-grafted polylysine, were reported by Kang et al., demonstrating efficient tumor-targeted drug delivery with low background tissue retention[21,27]. However, the tumor selectivity of these NCs is mainly due to their significantly reduced residence time in normal tissues, not the augmented tumor-homing ability. This suggests that by extending the tumor retention of renal-clearable organic NCs, much higher tumor selectivity can be achieved. Although targeting ligands can be introduced into the NC structure[28,29], this so-called active targeting strategy does not always ensure improved selectivity, unexpectedly inducing opsonization and consequent non-target accumulation, primarily *via* MPS uptake[30,31,32,33,34,35]. Therefore, delicate tailoring of the optimal NC structure is required for clinical success, balancing the targeting efficiency and off-target accumulation of renal-clearable NCs, which has yet to be investigated.

Colorectal cancer (CRC) is the third most commonly diagnosed cancer, with the second highest mortality rate and a constantly increasing incidence rate[36]. Adjuvant chemotherapy (ACT) after surgical resection is the current mainstay treatment for stage II and III CRC, resulting in improved overall survival and disease-free survival[37]. Despite its effectiveness, ACT is often limited by the severe toxicity of chemotherapeutic agents, such as 5-fluorouracil, irinotecan, and oxaliplatin[38,39]. To avoid the adverse effects of single-drug therapy, combination therapy with small doses of various drugs, such as FOLFIRI, FORFOX, CAPEOX, Optimox, and CONcePT, has been established as the standard regimen for CRC treatment to attain synergistic anticancer efficacy. However, such drug amalgamation still has not fully resolved the toxicity concerns[40], which warrants the development of innovative modalities to improve or replace existing ACT regimens[41].

Herein, we report novel designs for renal-clearable CD nanoplatforms that can promote tumor retention, without causing any off-target accumulation of imaging and therapeutic agents in CRC treatment. The relationship between structural design and target-to-background selectivity was elucidated by synthesizing 20 CD derivatives by varying the structures of the spacer and functional groups. Systematic evaluation of the CD library in terms of colloidal stability and *in vivo* distribution revealed a fine-tuned zwitterionic CD derivative, hepatkis-(6-deoxy-6-((phenylboronic acid-tetraethyleneglycol-l-glutamic acid N^{α}-sulfobetaine)-octaethyleneglycol-caproamide))-β-cyclodextrin (PBA-(ZW)-CD), as the optimal structure for targeted CRC therapy. Forming stable inclusion complexes, a fluorophore (adamantyl sulfocyanine 7) and two chemotherapeutic agents (doxorubicin and ulixertinib) were successfully loaded into PBA-(ZW)-CD for CRC imaging and treatment, respectively. Moreover, thorough evaluations were performed to verify whether these CD nanoplatforms facilitated the (1) selective delivery of imaging and chemotherapeutic agents to CRC tissues with substantially reduced off-target accumulation, (2) rapid clearance of NCs *via* the renal route, and (3) improvement of the efficacy and safety of CRC treatment.

2. Results And Discussion

2.1. Design, Synthesis, and Optimization of CD Derivatives

β-CD was selected as the core material to build organic renal-clearable NCs because of its several advantages, including biocompatibility and biodegradability, lack of pharmacological activity and immunogenicity, and a polyfunctional structure exhibiting hydrophobic cavity for host–guest interactions with various compounds, such as drugs and imaging probes[42]. Various charged moieties were introduced to the side chains of β-CD to reduce off-target accumulation, as the surface charge has a significant impact on the *in vivo* fate of NCs, especially those of ultrasmall sizes[19,20,21,27,28]. Sulfobetaine was adopted as a zwitterionic moiety because it can resist non-specific protein adsorption more efficiently than other amino acids[43]. Based on the general understanding of the structure–antifouling efficiency relationship of zwitterionic molecules[44], we prepared two types of sulfobetaine (compounds **2** and **4**) with different numbers of methylene groups between quaternary ammonium and carboxylic acid **(Figure S1)**. Succinic anhydride, betaine hydrochloride, and glycolic acid were used for the preparation of the negative, positive, and uncharged CD derivatives, respectively. Phenylboronic acid (PBA) was chosen as a tumor-targeting probe because it can recognize sialyl epitopes that are overexpressed in CRC cells[45]. The neutral charge of PBA at physiological pH was also suitable for minimizing the unintended charge effects by targeting ligands on the entire NC structure[46,47]. Glutamic acid was used as a tri-arm linker to tether both the charged moiety and the targeting ligand to the CD core.

Twenty CD derivatives (**CD 1–20**) were designed by modifying the charged moiety linked to the amine group of the glutamic acid linker (P1) and spacers between cyclodextrin and glutamic acid (P2), and glutamic acid and PBA (P3) **(**Fig. 1A**)**. Synthesis was performed through the following three main steps: (1) synthesis of PBA–P3 (zero-length or PEG_4)–glutamic acid (compounds **6** and **10**), (2) conjugation of (1) and CD–P2 (zero-length or spacers) (compounds **12**, **19**, **20**, **28**, and **30**), and (3) conjugation of (2) and P1 (charged moieties). Each module (A–F) was conjugated *via* amide coupling, and the detailed synthetic schemes are described in the Supporting Information **(Section S1.2 and Figure S2)**. Successful syntheses of the intermediates were confirmed using proton nuclear magnetic resonance (^{1}H-NMR) spectroscopy and mass spectrometry **(Figures S3–S7)**. The degrees of conjugation of PBA or spacers (PEG_n and caproic acid) to CD intermediates were calculated by comparing integration values of anomeric protons of CD (~ 4.8 ppm) and distinct signals of the conjugated compounds (8.0 and 1.3 ppm for PEG_n; 1.2–1.5 ppm for caproic acid; and 9.8, 6.8, and 1.3 ppm for PBA). The introduction of PBA was further confirmed *via* the alizarin red S test, wherein the CD intermediates (compounds **11**, **17**, **18**, **27**, and **29**) were nearly heptaconjugated **(Figure S8)**. In synthesis step (3), excess charged moieties were used to convert all the primary amines on the glutamic acid linker. The fluorescamine assay revealed that more than 98.8% of the primary amines were consumed within 48 h, indicating the complete conjugation of the charged moieties **(Figure S9)**. This result was further supported by the ^{1}H-NMR spectra of the final products, **CD 16–20 (Figure S10)**.

The foremost requirement for intravenous injections is colloidal stability in the bloodstream. It should be noted that CD derivatives may become more vulnerable to aggregation upon the formation of inclusion complexes with hydrophobic guest molecules. Thus, we screened out CD derivatives with poor colloidal stability in phosphate-buffered saline (PBS; high ionic strength condition) or fetal bovine serum (FBS;

bloodstream condition) based on turbidimetric analysis by measuring absorbance at 600 nm **(Figure S11A, summarized in** Fig. 1B**)**. CD derivatives with no spacers (*i.e.*, zero length) at P2 and P3 (**CD 1**, **2**, **4**, and **5**) exhibited precipitation when dispersed in PBS and FBS. The introduction of a short PEG_4 spacer at P2 was insufficient to secure colloidal stability in PBS (**CD 6**, **7**, **9**, and **10**); **CD 8**, **9**, and **10** were readily dissolved in FBS, while **CD 6** and **7** showed severe aggregation. These results can be attributed to the strong inter- and intramolecular interactions of the zwitterionic moieties rather than the inherent hydrophobicity of the CD molecules[48]. Accordingly, CD derivatives with longer spacers (PEG_8) at P2 (**CD 11**, **13**, **14**, and **15**) were dissolved in PBS and FBS. Interestingly, however, the A_2 module (compound **4**)-conjugated CD derivative (**CD 12**) precipitated in both media, even with the PEG_8 spacer. Thus, the A_1 module (compound **2**) was selected as the zwitterionic functional group for further study. Next, the length of the PEG spacer was extended to further improve the colloidal stability. For **CD 16**, PBA and A_1 were directly conjugated to glutamic acid and a long PEG_{12}-caproic acid spacer was inserted at P2. In contrast, **CD 17–20** were prepared by inserting a PEG_8-caproic acid spacer at P2 and the PEG_4 spacer at P3, hypothesizing that nearby sulfobetaine could hinder the sialic acid-targeting ability of PBA. As expected, **CD 16–20** were dissolved clearly in both media and exhibited no significant turbidity changes for 48 h, suggesting high colloidal stability after intravenous administration **(Figure S11B)**. Moreover, dynamic light scattering (DLS) analysis revealed that the hydrodynamic diameters (HDs) of **CD 16–20** were of renal-clearable size (5–6.6 nm), and the zeta potential of each CD derivative corresponded to the decorated charged moieties, supporting the successful synthesis of CD derivatives **(**Fig. 1C**)**.

2.2. Biodistribution of CD Derivatives

Adamantyl sulfocyanine 7 (ACy7) was synthesized as a fluorescence probe for the near-infrared fluorescence (NIRF) imaging-assisted biodistribution study of CD derivatives **(Figure S12A)**. Given its high affinity to the hydrophobic cavity of CD, ACy7 was successfully loaded onto **CD 16–20** by inducing host-guest interactions under aqueous conditions[49,50], resulting in stable CD/ACy7 inclusion complexes. Although **CD 11** and **14** had decent colloidal stability (Fig. 1B), gradual precipitation was observed in the presence of ACy7 **(Figure S12B)**, discouraging further evaluation of these two compounds.

Next, free ACy7 and **CD 16–20**/ACy7 inclusion complexes were intravenously administered to a CRC mouse model, and *ex vivo* imaging was performed 24 h post-injection **(**Fig. 1D**)**. In this study, HT-29 (human colorectal adenocarcinoma) was utilized because this cell line represents the traits of human CRC, including the high expression of sialyl Lewis A, a well-known target of PBA[51]. Compared to free Acy7, which showed non-selective organ distribution, **CD 16**/ACy7 (zwitterionic) exhibited significantly reduced lung and liver accumulation with increased kidney selectivity. These results imply that zwitterionic CD derivatives may reduce the off-target distribution or retention of cargo molecules and facilitate renal excretion. A similar phenomenon was observed in the case of **CD 17**/ACy7, another zwitterionic inclusion complex, wherein the average fluorescence intensity values of ACy7 in normal tissues were almost at the same levels as those of **CD 16**/ACy7. However, the tumor distribution efficiency of **CD 17**/ACy7 was 2.02-fold higher than that of **CD 16**/ACy7 ($p < 0.001$) **(**Fig. 1E**)**, even with

similar physicochemical properties (Fig. 1C). This result could be attributed to the insertion of the PEG_4 spacer between the PBA moiety and glutamic acid linker, reducing the possible interference of sulfobetaine in the PBA–sialic acid interaction (Fig. 1F). Although **CD 18**/ACy7, a negatively charged inclusion complex, displayed an overall high tumor-to-background ratio (TBR) comparable to that of **CD 17**/ACy7, the tumor distribution efficiency was 1.46-fold lower ($p < 0.01$) (Fig. 1E). Conversely, **CD 19**/ACy7 (positively charged) and **CD 20**/ACy7 (neutral) showed comparable tumor distribution efficiencies to **CD 17**/ACy7, but their TBR values were approximately 2-fold lower in all organs (Fig. 1G). Based on high TBR and tumor distribution efficiency, **CD 17**, hepatkis-(6-deoxy-6-((phenylboronic acid-tetraethyleneglycol-l-glutamic acid N^{α}-sulfobetaine)-octaethyleneglycol-caproamide))-β-cyclodextrin (PBA-(ZW)-CD), was selected as an optimized renal clearable CD derivative for further investigations.

2.3. Tumor Targetability, Pharmacokinetics, and Urinary Excretion of PBA-(ZW)-CD/ACy7

The structural components of PBA–(ZW)–CD are shown in Fig. 2A. The caproic acid linker enhanced hydrophobic interactions with guest molecules[52,53], and the PEG_8 spacer improved colloidal stability. Sulfobetaine, a zwitterionic functional group, reduces non-specific tissue binding[54,55]. The PEG_4 spacer between glutamic acid and PBA helped preserve the targeting ability of PBA. These features may translate into improved *in vivo* distribution profiles (Fig. 2B). Thus, we hypothesized that PBA-(ZW)-CD/ACy7 could be rapidly distributed throughout the body and selectively retained in tumor tissues *via* PBA–sialic acid interactions. In addition, the zwitterionic sulfobetaine moiety could reduce non-specific interactions between PBA-(ZW)-CD and normal tissues; thus, the clearance of ACy7 may be accelerated *via* the renal route, further enhancing tumor selectivity.

Prior to verifying the targetability of PBA-(ZW)-CD *in vivo*, enhancement in the cellular uptake of PBA-(ZW)-CD/ACy7 *via* PBA–sialic acid interaction was confirmed in HT-29 cells by fluorescence microscopy **(Figure S13A)**. Notably, the cellular uptake efficiency of PBA-(ZW)-CD/ACy7 was compromised in the presence of free sialic acid, a competitive inhibitor, suggesting the involvement of PBA–sialic acid interactions in the cellular uptake of PBA-(ZW)-CD. Similarly, flow cytometry analyses were performed on HT-29 cells treated with the inclusion complex of adamantyl sulfocyanine 5 **(Figure S12A; Figure S13B)**, and the results corresponded well with the fluorescence microscopy data, supporting the use of PBA as an HT-29 targeting moiety.

The tumor targeting ability of PBA-(ZW)-CD/ACy7 was investigated in HT-29 tumor-xenograft mice using real-time NIRF imaging (Fig. 2C). In the early phase (~ 2 h), intravenously administered ACy7 and PBA-(ZW)-CD/ACy7 were both distributed throughout the body with no tumor selectivity. However, after rapid renal excretion of PBA-(ZW)-CD, which was verified in a preliminary study with sulfocyanine 7-conjugated PBA-(ZW)-CD (*i.e.*, *via* covalent bond) **(Figure S14)**, the PBA-(ZW)-CD/ACy7 inclusion complex-treated mice exhibited distinct fluorescence signals in the tumor and kidney regions in whole-body imaging (Fig. 2C). Furthermore, the TBR of PBA-(ZW)-CD/ACy7 exceeded 2, the standard cut-off value for tumor

detection[56], at 8 h post-injection and continuously increased for the next 16 h, whereas free ACy7 showed TBR values less than 2 throughout the experimental period (Fig. 2D). The high TBR of PBA-(ZW)-CD/ACy7 can be attributed to prolonged tumor retention and accelerated elimination from normal tissues. From a clinical perspective, determining the tumor margin is of paramount importance for the accurate surgical resection of CRC, especially in laparoscopic or robot-assisted operations[56,57,58]. To evaluate the applicability of PBA-(ZW)-CD/ACy7 in image-guided surgery, PBA-(ZW)-CD/ACy7 was injected into the tail vein of an orthotopic CRC model, which was prepared by subserosal inoculation of HT-29 cells in the cecum after laparotomy. At 24 h post-injection, PBA-(ZW)-CD/ACy7 showed high TBR values of approximately 4 against adjacent normal tissues, including the small intestine, colon, and muscle, providing accurate tumor margins for resection (Fig. 2E and 2F).

The pharmacokinetic properties of PBA-(ZW)-CD/ACy7 were investigated *via* time-course blood sampling and ACy7 quantification **(Figure S15)**. Exhibiting biphasic decay, free ACy7 and PBA-(ZW)-CD/ACy7 showed similar distribution half-lives ($t_{1/2\alpha}$; 4.2 and 3.0 min, respectively). This result suggests that PBA-(ZW)-CD/ACy7 can be distributed to the whole body as quickly as free ACy7, as observed in the *in vivo* imaging study (Fig. 2C). However, in the elimination phase, PBA-(ZW)-CD/ACy7 had a significantly shorter elimination half-life ($t_{1/2\beta}$; 52.5 min) than free ACy7 (92.5 min). Considering comparable exposure, the reduced $t_{1/2\beta}$ value could result from the lower volume of distribution (V_d) of the inclusion complex (5.6 mL) compared to that of the free dye (7.6 mL), which also implies reduced non-specific binding of ACy7 in normal tissues. Although the total body clearance values of free dye (0.08 mL min^{-1}) and inclusion complex (0.10 mL min^{-1}) were almost the same, the cumulative urinary excretion of PBA-(ZW)-CD/ACy7 was 2.3-fold higher than that of free ACy7, which suggests that PBA-(ZW)-CD may facilitate the renal excretion of cargo molecules (Fig. 2G).

2.4. Preparation and Characterization of PBA-(ZW)-CD/Drug Inclusion Complexes

PBA-(ZW)-CD/drug inclusion complexes were prepared with two chemotherapeutic agents, doxorubicin (DOX) and ulixertinib (UXT) to assess the potential of CRC-targeted combination therapy. Generally, the use of DOX is discouraged in CRC treatment, as DOX activates the extracellular signal-regulated kinase (ERK)-1/2 signaling pathway and induces drug resistance. However, combination therapy with UXT, a potent first-in-class ERK1/2 inhibitor, may help overcome DOX resistance and further enhance therapeutic efficacy (Fig. 3A)[59,60,61,62,63]. As both drugs were poorly soluble in aqueous media, a co-solvent of dimethyl sulfoxide and water was used to solubilize the drugs with PBA-(ZW)-CD to induce host–guest interactions. After lyophilization, water-soluble PBA-(ZW)-CD/drug inclusion complexes were obtained at molar ratios of drug to PBA-(ZW)-CD of approximately 1 and 2 for DOX and UXT, respectively (Fig. 3B). The drug contents of PBA-(ZW)-CD/DOX and PBA-(ZW)-CD/DOX were 5.10 ± 0.13% and 7.91 ± 0.14%, which were close to the theoretical values of 5.26% and 8.13%, respectively.

The formation of PBA-(ZW)-CD/drug inclusion complexes was investigated using ^{1}H-NMR (Fig. 3C). Although the peaks of CD protons engaging in the host–guest interaction (*i.e.*, protons in the CD cavity) overlapped with strong PEG signals at 3.5–3.9 ppm, we could observe slight changes in the chemical shifts of DOX (red arrows) and UXT (blue arrows) after complexation[64,65]. These intermolecular correlations were further confirmed by rotating frame Overhauser enhancement spectroscopy (ROESY) (Fig. 3D). The ROESY spectrum of PBA-(ZW)-CD/DOX revealed dipolar couplings between the aromatic proton Ha of DOX and H1 protons of PBA-(ZW)-CD, indicating that the anthraquinone rings of DOX were internalized in the cyclodextrin cavity. The PBA-(ZW)-CD/UXT spectrum also displayed interactions between the protons Hb, Hc, and Hd of UXT and the inner cavity protons H2 and H3 of PBA-(ZW)-CD, supporting inclusion complex formation.

The HDs of the inclusion complexes were measured using DLS to confirm whether PBA-(ZW)-CD maintained its renal-clearable size after drug loading (Fig. 3E). As shown in the number-weighted HD distribution, PBA-(ZW)-CD/DOX had a mean HD of 13.04 ± 3.85 nm at pH 7.4. The slight increase in HD compared to that of the blank PBA-(ZW)-CD could be attributed to concentration-dependent (*i.e.*, reversible) coordination between the primary amine of DOX and boronic acid of PBA-(ZW)-CD[66]. Since the coordination weakens at acidic pH, the mean HD of PBA-(ZW)-CD/DOX decreased to 7.09 ± 0.26 nm at pH 5.5, which is almost the same value of blank PBA-(ZW)-CD HD (6.58 ± 0.27 nm; Fig. 1C). However, PBA-(ZW)-CD/UXT showed comparable HD distributions at pH 5.5 and 7.4, displaying mean HDs of 6.30 ± 0.11 nm and 6.30 ± 0.09 nm, respectively, which implies the lesser influence of acidity. A similar phenomenon was observed in drug release tests performed at pH 5.5 and 7.4 (Fig. 3F). Due to the DOX–boronic acid coordination, the cumulative DOX release from the inclusion complex reached only 4.9 ± 0.9% even after 24 h incubation at pH 7.4. However, at pH 5.5, the cumulative DOX release significantly increased to 21.3 ± 0.1% ($p < 0.005$), which could translate into selective drug exposure to tumor tissues, considering the acidic tumor microenvironment (TME). PBA-(ZW)-CD/UXT also showed statistically significant pH-dependency in its release profile, but the cumulative drug release under each condition showed only a 10% difference, displaying 38.9 ± 2.8% and 27.9 ± 1.6% at pH 5.5 and 7.4, respectively. The zeta potential of both inclusion complexes increased at acidic pH due to the ionization of the guest drug while maintaining zwitterionic properties at pH 7.4 (Fig. 3E), which also explains the enhanced drug release of both inclusion complexes at pH 5.5.

2.5. Biodistribution of PBA-(ZW)-CD/Drug Inclusion Complexes

The biodistribution of PBA-(ZW)-CD/drug inclusion complexes was assessed in subcutaneous HT-29 tumor xenograft mice in comparison with that of free drugs, wherein the drug amounts deposited in major organs, muscles, and tumors were determined after intravenous administration of the drug solution or inclusion complex at a dose of 5 mg kg^{-1}. As expected from the biodistribution profiles of PBA-(ZW)-CD/ACy7 (Fig. 1D), DOX exposure to normal tissues (*i.e.*, off-target) in the distribution phase was drastically decreased when treated with PBA-(ZW)-CD/DOX (Fig. 4A). Notably, the DOX amount in the

heart at 2 h in the inclusion complex group was 6.5-fold lower than that in the free drug group ($p < 0.001$). Moreover, in the muscle tissue, the DOX level of the inclusion complex group was below the detection limit (< 200 ng g^{-1} tissue) even at 0.5 h post injection, while the free DOX group exhibited 2.73 ± 0.30 μg g^{-1} tissue. Considering that cardiotoxicity and skeletal muscle atrophy are the major side effects of DOX that limit its application to CRC[67,68,69,70], the improved biodistribution profile *via* PBA-(ZW)-CD complexation could enhance the chances of future clinical translation. In the tumor tissue, although both free DOX and PBA-(ZW)-CD/DOX exhibited similar exposure at 0.5 h, PBA-(ZW)-CD/DOX had prolonged tumor retention compared to free DOX, resulting in 2.0-fold higher DOX accumulation at 8 h ($p < 0.005$).

Unlike DOX, which non-specifically binds to various biomacromolecules, UXT exhibited the expected biodistribution profile when formulated as PBA-(ZW)-CD/UXT (Fig. 4B). PBA-(ZW)-CD/UXT showed rapid clearance in the normal tissues, with UXT amounts remaining in the heart, lungs, kidneys, and liver less than 0.65 μg g^{-1} tissue within 2 h, which were 8.0-, 17.0-, 5.6-, and 13.6-fold lower values than those of free UXT solution, respectively. In the tumor tissues, however, PBA-(ZW)-CD/UXT displayed a 2.1-fold higher accumulation of UXT than free UXT at 8 h post-injection ($p < 0.05$). These findings clearly indicate that PBA-(ZW)-CD can enhance the tumor retention of guest drugs and reduce their off-target accumulation in normal tissues, as in the case of PBA-(ZW)-CD/ACy7 (cf. Section 2.2).

Enhancement of the average drug concentration in tumor tissues could be one of the critical elements for successful tumor-targeted drug delivery. However, one cannot underestimate the importance of homogenous drug distribution throughout the tumor mass, as the presence of cancer cells that are poorly exposed to anticancer agents can result in tumor relapse[71,72,73]. Conventional NCs utilizing the EPR effect suffer from the issue of reduced convection in the TME owing to their large particle size[74,75,76,77]. PBA-(ZW)-CD/drug inclusion complexes could evade this issue given their ultrasmall size and zwitterionic surface charge. As observed in the *ex vivo* matrix-assisted laser desorption ionization-mass spectrometry imaging (MALDI-MSI) (Fig. 4C), the intratumoral DOX (*m/z* 544.6) and UXT (*m/z* 434.7) signals in the inclusion complex-treated group exhibited a comparable spatial intensity distribution (as the coefficient of variation) to those of the solution-treated group, suggesting that PBA-(ZW)-CD/drug was as highly tumor-penetrable as a free drug solution (Fig. 4D). In addition, the average intensity values of both drugs were significantly higher in the PBA-(ZW)-CD/drug groups than in the corresponding solution groups (Fig. 4E), which correlates well with the biodistribution study performed with tissue homogenates (Fig. 4A and 4B).

The unique pharmacokinetic properties of PBA-(ZW)-CD, which are rarely observed in other clinical reports[78], are summarized as follows: (1) PBA-(ZW)-CD may control the biodistribution of cargo molecules in an opposite manner depending on the deposition site, showing decreased and increased clearance in tumor and normal tissues, respectively, and (2) PBA-(ZW)-CD/drug inclusion complexes may penetrate the TME as readily as free drug solutions, promoting homogeneous drug delivery throughout the tumor mass. Based on these findings, we hypothesized that PBA-(ZW)-CD/drug inclusion complexes

could simultaneously improve the apparent potency and reduce the potential toxicity of anticancer agents, enabling high-dose administration and subsequent enhancement of therapeutic efficacy.

2.6. PBA-(ZW)-CD/Drug-Assisted Single-Drug and Combination Therapies in HT-29 Xenograft Model

Encouraged by the remarkable biodistribution profiles of PBA-(ZW)-CD, the *in vivo* antitumor efficacy of each PBA-(ZW)-CD/drug inclusion complex was evaluated in the heterotopic HT-29 xenograft mouse model. As a preliminary study, the *in vitro* and *in vivo* toxicity of blank PBA-(ZW)-CD was evaluated. In HT-29 cells, PBA-(ZW)-CD showed negligible cytotoxicity at physiologically-relevant concentrations (~ 500 μg mL^{-1}) **(Figure S16A)**. Moreover, single and repeated (three times) intravenous administration of an excess amount of PBA-(ZW)-CD (270 mg kg^{-1} per administration) induced no significant deviation in the complete blood counts of mice without observable changes in vital signs or behavioral expressions of pain **(Figure S16B)**.

To evaluate the tumor-suppressive efficiency of PBA-(ZW)-CD/DOX and its potential to reduce the adverse effects of DOX, the dose was set at 5 mg kg^{-1}, wherein significant systemic toxicity and cardiotoxicity of DOX have been reported[79,80]. As shown in **Figure S17**, the tumor volume of the PBA-(ZW)-CD/DOX group was significantly smaller than that of the other groups ($p < 0.005$). The body weight of the DOX solution group was significantly lower than that of the other groups, indicating that a high dose of free DOX caused severe systemic toxicity. However, there was no noticeable change in body weight of the PBA-(ZW)-CD/DOX group during treatment ($p < 0.001$). Similarly, PBA-(ZW)-CD/UXT also showed a significant improvement in tumor growth inhibition at the therapeutic dose (5 mg kg^{-1}) ($p < 0.001$), but systemic toxicity in terms of body weight change was not observed in any group **(Figure S18)**. Since the inclusion complex had a marginally higher cytotoxicity than the corresponding free drug **(Figure S19)**, its highly enhanced antitumor efficacy *in vivo* could mainly result from improved biodistribution.

Next, we performed a combination therapy with PBA-(ZW)-CD/DOX and PBA-(ZW)-CD/UXT in the same mouse model. The mice were divided into six groups, including PBS, blank PBA-(ZW)-CD, DOX or UXT monotherapy (solution), and DOX + UXT combination therapy (solution or inclusion complex), and intravenously injected with each intervention every three days five times, and the doses of DOX and UXT were reduced to 3 mg kg^{-1}, expecting the synergistic effect of DOX and UXT combination. As observed in the tumor growth profile **(**Fig. 5A**)**, the combination of DOX and UXT solutions exhibited enhanced antitumor efficacy on average when compared to monotherapy with each drug, but no statistically significant difference was found between the DOX + UXT solution and DOX solution groups ($p > 0.05$). However, the combination of inclusion complexes showed dramatically improved tumor growth inhibition compared to the other groups, of which the average tumor volume on day 14 was 2.1-fold smaller than that in the DOX + UXT solution group ($p < 0.05$). A similar tendency was observed in the dissected tumor weight data **(**Fig. 5B**)**, where the PBA-(ZW)-CD/DOX + PBA-(ZW)-CD/UXT group displayed the lowest tumor weight compared to the other groups, showing a 2.9-fold lower average tumor weight on day 14

compared to that of the DOX + UXT solution group ($p < 0.05$). The superior antitumor efficacy of the PBA-(ZW)-CD/drug combination could be explained by the improved drug distribution to the tumor tissue spatially and temporally enough to induce synergistic effects between DOX and UXT (cf. Section 2.5). Meanwhile, the mice in all groups did not lose body weight significantly during the treatment (Fig. 5C) and showed no abnormal changes in blood biochemistry **(Figure S20)**, indicating negligible systemic toxicity.

2.7. PBA-(ZW)-CD/Drug Combination Therapy in Orthotopic CRC Model

Antitumor efficacy of the PBA-(ZW)-CD/drug-assisted combination therapy was evaluated in an orthotopic CRC model. One week after the inoculation of luciferase-expressing HT-29 (HT-29/Luc) cells into the cecum, the mice were intravenously administered PBS (no intervention), DOX + UXT (solution), or PBA-(ZW)-CD/DOX + PBA-(ZW)-CD/UXT every three days for five times at a dose of 3 mg kg^{-1} for each drug. Bioluminescence imaging revealed that both solution- and inclusion complex-based combination therapies significantly reduced tumor growth compared to no intervention (Fig. 5D). Notably, PBA-(ZW)-CD/drug combination therapy had a much higher tumor inhibitory efficacy than solution therapy, displaying a 4.2-fold lower bioluminescence intensity on day 14 ($p < 0.005$) (Fig. 5E).

Unlike the heterotopic model prepared by the subcutaneous injection of HT-29 cell suspension (cf. section 2.6), the orthotopic CRC model prepared *via* laparotomy exhibited lower tolerability to solution-based combination therapy, with the average body weight reduced to 88.9% of the non-intervention (PBS) group ($p < 0.01$) (Fig. 5F). However, no weight loss was observed in the PBA-(ZW)-CD/drug combination group, implying that PBA-(ZW)-CD reduced the systemic toxicity of ACT after surgical resection. At the end of the efficacy test, tumor tissues and major organs, including the heart, kidneys, liver, lungs, and spleen, were dissected and subjected to hematoxylin and eosin staining. As shown in Fig. 5G, no detrimental changes were observed in normal tissues, indicating that PBA-(ZW)-CD can minimize the dose-limiting toxicity of anticancer agents. Terminal deoxynucleotidyl transferase dUTP nick-end labeling staining was also performed on the tumor tissues (Fig. 5G), which revealed that PBA-(ZW)-CD/drug combination therapy induced a higher degree of apoptosis than solution-based combination therapy. This result correlated well with the antitumor efficacy data (Fig. 5A and 5E).

3. Conclusions

We presented a delicately tailored design of renal-clearable zwitterionic CD, namely PBA-(ZW)-CD, for CRC-selective imaging and drug delivery. Twenty CD derivatives were prepared by modifying the charged moieties and spacers to improve their colloidal stability and *in vivo* pharmacokinetic behavior. CRC targetability, organ distribution, and renal clearance of CD derivatives were screened in the form of ACy7 inclusion complexes, from which PBA-(ZW)-CD was selected as the optimized structure with enhanced tumor selectivity and reduced off-target accumulation. Given its high biocompatibility, PBA-(ZW)-CD/drug inclusion complexes of DOX and UXT were fabricated and applied in combination therapy for CRC.

Notably, PBA-(ZW)-CD enhanced the tumor retention of drugs, while facilitating their elimination in normal tissues. Additionally, the improved antitumor efficacies of PBA-(ZW)-CD/drug-assisted single-drug and combination therapies were demonstrated in various CRC models. Therefore, PBA-(ZW)-CD may be used as a promising CRC-targeting nanoplatform with high potential for clinical translation.

Declarations

Data availability

All relevant data of this study are available within the paper and its Supplementary Information.

Acknowledgements

This work was supported by the National Research Foundation of Korea (NRF) grants funded by the Ministry of Science and ICT (grant nos. NRF-2021R1C1C1009320, NRF-2018R1A5A2024425, NRF-2018M3A7B4071203, NRF-2020R1A2C2099983, and NRF-2018H1A2A1062046).

Conflict of Interest

The authors declare no conflict of interest.

References

1. Blanco, E. et al. Principles of nanoparticle design for overcoming biological barriers to drug delivery. Nat. Biotechnol. **33**, 941–951 (2015)
2. Yu, M. X. & Zheng, J. Clearance Pathways and Tumor Targeting of Imaging Nanoparticles. ACS Nano **9**, 6655–6674 (2015).
3. Nurunnabi, M. et al. In Vivo Biodistribution and Toxicology of Carboxylated Graphene Quantum Dots. ACS Nano **7**, 6858–6867 (2013).
4. Li, B. & Lane, L.A. Probing the biological obstacles of nanomedicine with gold nanoparticles. Wiley Interdiscip. Rev. Nanomed. Nanobiotechnol. **11**, e1542 (2019).
5. Zhang, Y.N. et al. Nanoparticle-liver interactions: Cellular uptake and hepatobiliary elimination. J. Control. Release **240**, 332–348 (2016).
6. Longmire, M. et al. Clearance properties of nano-sized particles and molecules as imaging agents: considerations and caveats. Nanomedicine (Lond) **3**, 703–717 (2008).
7. Cheng, Y.H. et al. Meta-Analysis of Nanoparticle Delivery to Tumors Using a Physiologically Based Pharmacokinetic Modeling and Simulation Approach. ACS Nano **14**, 3075–3095 (2020).

8. Lammers, T. Macro-nanomedicine: Targeting the big picture. J. Control. Release **294**, 372–375 (2019).
9. Choi, H.S. et al. Renal clearance of quantum dots. Nat. Biotechnol. **25**, 1165–1170 (2007).
10. Liu, J.B. et al Renal clearable inorganic nanoparticles: a new frontier of bionanotechnology. Mater. Today **16**, 477–486 (2013).
11. Zhou, C. et al. Luminescent Gold Nanoparticles with Efficient Renal Clearance. Angew. Chem., Int. Ed. Engl. **50**, 3168–3172 (2011).
12. Zhou, C. et al. Near-Infrared Emitting Radioactive Gold Nanoparticles with Molecular Pharmacokinetics. Angew. Chem., Int. Ed. Engl. **51**, 10118–10122 (2012).
13. Liu, J.B. et al. Passive Tumor Targeting of Renal-Clearable Luminescent Gold Nanoparticles: Long Tumor Retention and Fast Normal Tissue Clearance. J. Am. Chem. Soc. **135**, 4978–4981 (2013).
14. Burns, A.A. et al. Fluorescent Silica Nanoparticles with Efficient Urinary Excretion for Nanomedicine. Nano Lett **9**, 442–448 (2009).
15. Ruggiero, A. et al. Paradoxical glomerular filtration of carbon nanotubes. *Proc. Natl. Acad. Sci. U. S. A.* **107**, 12369–12374. (2010)
16. Peng, C.Q. et al. Correlating Anticancer Drug Delivery Efficiency with Vascular Permeability of Renal Clearable Versus Non-renal Clearable Nanocarriers. Angew. Chem., Int. Ed. Engl. **58**, 12076–12080 (2019).
17. Peng, C.Q. et al. Renal clearable nanocarriers: Overcoming the physiological barriers for precise drug delivery and clearance. J. Control. Release **322**, 64–80 (2020)
18. Peng, C. et al. Tuning the In Vivo Transport of Anticancer Drugs Using Renal-Clearable Gold Nanoparticles. Angew. Chem., Int. Ed. Engl. **58**, 8479–8483 (2019).
19. Liu, J. et al. PEGylation and zwitterionization: pros and cons in the renal clearance and tumor targeting of near-IR-emitting gold nanoparticles. Angew. Chem., Int. Ed. Engl. **52**, 12572–12576 (2013).
20. Kang, H. et al. Renal Clearable Theranostic Nanoplatforms for Gastrointestinal Stromal Tumors. Adv. Mater. **32**, e1905899 (2020).
21. Kang, H. et al. Renal Clearable Organic Nanocarriers for Bioimaging and Drug Delivery. Adv. Mater. **28**, 8162–8168 (2016).
22. Wang, H. et al. Renal-Clearable Porphyrinic Metal-Organic Framework Nanodots for Enhanced Photodynamic Therapy. ACS Nano **13**, 9206–9217 (2019).
23. Choi, H.S. et al. Design considerations for tumour-targeted nanoparticles. Nat. Nanotechnol. **5**, 42–47 (2010).
24. Zhou, C. et al. Luminescent gold nanoparticles with efficient renal clearance. Angew. Chem., Int. Ed. Engl. **50**, 3168–3172 (2011).
25. Huang, H. et al. Inorganic nanoparticles in clinical trials and translations. Nano Today **35**, 100972 (2020).

26. Missaoui, W.N. et al. Toxicological status of nanoparticles: What we know and what we don't know. Chem. Biol. Interact. **295**, 1–12 (2018).
27. Kang, H. et al. Size-Dependent EPR Effect of Polymeric Nanoparticles on Tumor Targeting. Adv. Healthc. Mater. **9**, 1901223 (2020).
28. Choi, H.S. et al. Targeted zwitterionic near-infrared fluorophores for improved optical imaging. Nat. Biotechnol. **31**, 148–153 (2013).
29. Verbeek, F.P.R. et al. Near-Infrared Fluorescence Imaging of Both Colorectal Cancer and Ureters Using a Low-Dose Integrin Targeted Probe. Ann. Surg. Oncol. **21**, S528-S537 (2014).
30. Sofias, A.M. et al. Tumor Targeting by alpha(v)beta(3)-Integrin-Specific Lipid Nanoparticles Occurs via Phagocyte Hitchhiking. ACS Nano **14**, 7832–7846 (2020).
31. McNeeley, K.M, et al. Decreased circulation time offsets increased efficacy of PEGylated nanocarriers targeting folate receptors of glioma. Nanotechnology, **18**, 385101 (2007).
32. Shuhendler, A.J. et al. A Novel Solid Lipid Nanoparticle Formulation for Active Targeting to Tumor alpha(v)beta(3) Integrin Receptors Reveals Cyclic RGD as A Double-Edged Sword. Adv. Healthc. Mater. **1**, 600–608 (2012).
33. Cheng, W.W. & Allen, T.M. Targeted delivery of anti-CD19 liposomal doxorubicin in B-cell lymphoma: a comparison of whole monoclonal antibody, Fab' fragments and single chain Fv. J. Control. Release **126**, 50–58 (2008).
34. Zhang, Y. et al. Strategies and challenges to improve the performance of tumor-associated active targeting. J. Mater. Chem. B **8**, 3959–3971 (2020).
35. Zhao, Z. et al. Targeting Strategies for Tissue-Specific Drug Delivery. Cell **181**, 151–167 (2020).
36. Bray, F. et al. Global cancer statistics 2018: GLOBOCAN estimates of incidence and mortality worldwide for 36 cancers in 185 countries. CA Cancer J. Clin. **70**, 313–313 (2020).
37. McCleary, N.J. et al. Personalizing Adjuvant Therapy for Stage II/III Colorectal Cancer. Am. Soc. Clin. Oncol. Educ. Book. **37**, 232–245 (2017).
38. Jalaeikhoo, H. et al. Effectiveness of adjuvant chemotherapy in patients with Stage II colorectal cancer: A multicenter retrospective study. J. Res. Med. Sci. **24**, 39 (2019).
39. Taieb, J. & Gallois, C. Adjuvant Chemotherapy for Stage III Colon Cancer. Cancers **12**, 2679 (2020).
40. Braun, M.S. & Seymour, M.T. Balancing the efficacy and toxicity of chemotherapy in colorectal cancer. Ther. Adv. Med. Oncol. **3**, 43–52 (2011).
41. Xie, Y.H. et al. Comprehensive review of targeted therapy for colorectal cancer. Signal Transduct. Target. Ther. **5**, 22 (2020).
42. Benito, J.M. et al. Optimizing saccharide-directed molecular delivery to biological receptors: Design, synthesis, and biological evaluation of glycodendrimer - Cyclodextrin conjugates. J. Am. Chem. Soc. **126**, 10355–10363 (2004).
43. Shao, Q. & Jiang S.Y. Influence of Charged Groups on the Properties of Zwitterionic Moieties: A Molecular Simulation Study. J. Phys. Chem. B **118**, 7630–7637 (2014).

44. van Andel, E. et al. Systematic Comparison of Zwitterionic and Non-Zwitterionic Antifouling Polymer Brushes on a Bead-Based Platform. Langmuir **35**, 1181–1191 (2019).
45. Deshayes, S. et al. Phenylboronic Acid-Installed Polymeric Micelles for Targeting Sialylated Epitopes in Solid Tumors. J. Am. Chem. Soc. **135**, 15501–15507 (2013).
46. Lee, J.Y. et al. Phenylboronic Acid-Decorated Chondroitin Sulfate A-Based Theranostic Nanoparticles for Enhanced Tumor Targeting and Penetration. Adv. Funct. Mater. **25**, 3705–3717 (2015).
47. Liu, H. et al. Dual-responsive surfaces modified with phenylboronic acid-containing polymer brush to reversibly capture and release cancer cells. J. Am. Chem. Soc. **135**, 7603–7609 (2013).
48. Blackman, L.D. et al. An introduction to zwitterionic polymer behavior and applications in solution and at surfaces. Chem. Soc. Rev. **48**, 757–770 (2019).
49. Ooi, H.W. et al. Multivalency Enables Dynamic Supramolecular Host-Guest Hydrogel Formation. Biomacromolecules, **21**, 2208–2217 (2020).
50. Lee, D.W. et al. Supramolecular assembly based on host-guest interaction between beta-cyclodextrin and adamantane for specifically targeted cancer imaging. J. Ind. Eng. Chem. **57**, 37–44 (2018).
51. Xu, X.D. et al. In situ recognition of cell-surface glycans and targeted imaging of cancer cells. Sci. Rep. **3**, 2679 (2013).
52. Okamatsu, A. et al. Design and Evaluation of Folate-Appended alpha-, beta-, and gamma-Cyclodextrins Having a Caproic Acid as a Tumor Selective Antitumor Drug Carrier in Vitro and in Vivo. Biomacromolecules **14**, 4420–4428 (2013).
53. Okamatsu, A. et al. Folate-Appended beta-Cyclodextrin as a Promising Tumor Targeting Carrier for Antitumor Drugs in Vitro and in Vivo. Bioconjugate Chem **24**, 724–733 (2013).
54. Hyun, H. et al. 700-nm Zwitterionic Near-Infrared Fluorophores for Dual-Channel Image-Guided Surgery. Mol. Imaging. Biol. **18**, 52–61 (2016).
55. Shao, Q. & Jiang, S. Influence of Charged Groups on the Properties of Zwitterionic Moieties: A Molecular Simulation Study. J. Phys. Chem. B **118**, 7630–7637 (2014).
56. Galema, H.A. et al. Fluorescence-guided surgery in colorectal cancer; A review on clinical results and future perspectives. Eur. J. Surg. Oncol. **48**, 810–821 (2022).
57. Tringale, K.R. et al. Image-guided surgery in cancer: A strategy to reduce incidence of positive surgical margins. Wiley Interdiscip. Rev. Syst. Biol **10**, e1412 (2018).
58. Keller, D.S. et al. Indocyanine green fluorescence imaging in colorectal surgery: overview, applications, and future directions. Lancet Gastroenterol. Hepatol. **2**, 757 (2017).
59. Shukla, A. et al. Blocking of ERK1 and ERK2 sensitizes human mesothelioma cells to doxorubicin. Mol. Cancer **9**, 314 (2010).
60. Salaroglio, I.C. et al. ERK is a Pivotal Player of Chemo-Immune-Resistance in Cancer. Int. J. Mol. Sci. **20**, 2505 (2019).
61. Christowitz, C. et al. Mechanisms of doxorubicin-induced drug resistance and drug resistant tumour growth in a murine breast tumour model. BMC Cancer **19**, 757 (2019).

62. Ortiz, R. et al. Nanomedicine to Overcome Multidrug Resistance Mechanisms in Colon and Pancreatic Cancer: Recent Progress. Cancers **13**, 2058 (2021).
63. Kim, D.H. et al. Effects of kefir on doxorubicin-induced multidrug resistance in human colorectal cancer cells. J. Funct. Food. **78**, 104371 (2021).
64. Yuan, C. et al. Inclusion complex of astaxanthin with hydroxypropyl-beta-cyclodextrin: UV, FTIR, H-1 NMR and molecular modeling studies. Carbohydr. Polym. **89**, 492–496 (2012).
65. Hamdi, H. et al. Spectroscopic studies of inclusion complex of beta-cyclodextrin and benzidine diammonium dipicrate. Spectrochim. Acta A Mol. Biomol. Spectrosc. **75**, 32–36 (2010).
66. Lv, S. et al. High Drug Loading and Sub-Quantitative Loading Efficiency of Polymeric Micelles Driven by Donor-Receptor Coordination Interactions. J. Am. Chem. Soc. **140**, 1235–1238 (2018).
67. Hiensch, A.E. et al. Doxorubicin-induced skeletal muscle atrophy: Elucidating the underlying molecular pathways. Acta Physiol. **229**, e13400 (2020).
68. Ou, H.C. et al. Low-level laser prevents doxorubicin-induced skeletal muscle atrophy by modulating AMPK/SIRT1/PCG-1alpha-mediated mitochondrial function, apoptosis and up-regulation of pro-inflammatory responses. Cell Biosci. **11**, 200 (2021).
69. Henriksen, P.A. Anthracycline cardiotoxicity: an update on mechanisms, monitoring and prevention. Heart **104**, 971–977 (2018).
70. Tian, Z. et al. High cumulative doxorubicin dose for advanced soft tissue sarcoma. BMC Cancer **20**, 1139 (2020).
71. Tredan, O. et al. Drug resistance and the solid tumor microenvironment. J. Natl. Cancer Inst. **99**, 1441–1454 (2007).
72. Torok, S. et al. Limited Tumor Tissue Drug Penetration Contributes to Primary Resistance against Angiogenesis Inhibitors. Theranostics **7**, 400–412 (2017).
73. Ziemys, A. et al. Progression-dependent transport heterogeneity of breast cancer liver metastases as a factor in therapeutic resistance. J. Control. Release **291**, 99–105 (2018).
74. Cabral, H. et al. Accumulation of sub-100 nm polymeric micelles in poorly permeable tumours depends on size. Nat. Nanotechnol. **6**, 815–823 (2011).
75. Zhou, Q. et al. Enzyme-activatable polymer-drug conjugate augments tumour penetration and treatment efficacy. Nat. Nanotechnol. **14**, 799–809 (2019).
76. Jain, R.K. & Stylianopoulos, T. Delivering nanomedicine to solid tumors. Nat. Rev. Clin. Oncol. **7**, 653–664 (2010).
77. Waite, C.L. & Roth, C.M. Nanoscale drug delivery systems for enhanced drug penetration into solid tumors: current progress and opportunities. Crit. Rev. Biomed. Eng. **40**, 21–41 (2012).
78. Sun, D.X. et al. What Went Wrong with Anticancer Nanomedicine Design and How to Make It Right. ACS Nano **14**,12281–12290 (2020).
79. Shim, M.K. et al. Carrier-free nanoparticles of cathepsin B-cleavable peptide-conjugated doxorubicin prodrug for cancer targeting therapy. J. Control. Release **294**, 376–389 (2019).

80. Yang, S. et al. Cancer-activated doxorubicin prodrug nanoparticles induce preferential immune response with minimal doxorubicin-related toxicity. Biomaterials **272**, 120791 (2021).
81. Dwivedi, R. et al. Design of therapeutically improved analogue of the antimicrobial peptide, indolicidin, using a glycosylation strategy. Amino Acids, **51**, 1443–1460 (2019).
82. Kasashima, H. et al. Mouse model of colorectal cancer: orthotopic co-implantation of tumor and stroma cells in cecum and rectum. STAR Protoc. **2**, 100297 (2021).
83. Gontijo, S.M.L. et al. Erlotinib/hydroxypropyl-beta-cyclodextrin inclusion complex: characterization and in vitro and in vivo evaluation. J. Incl. Phenom. Macrocycl. Chem. **83**, 267–279 (2015).

Figures

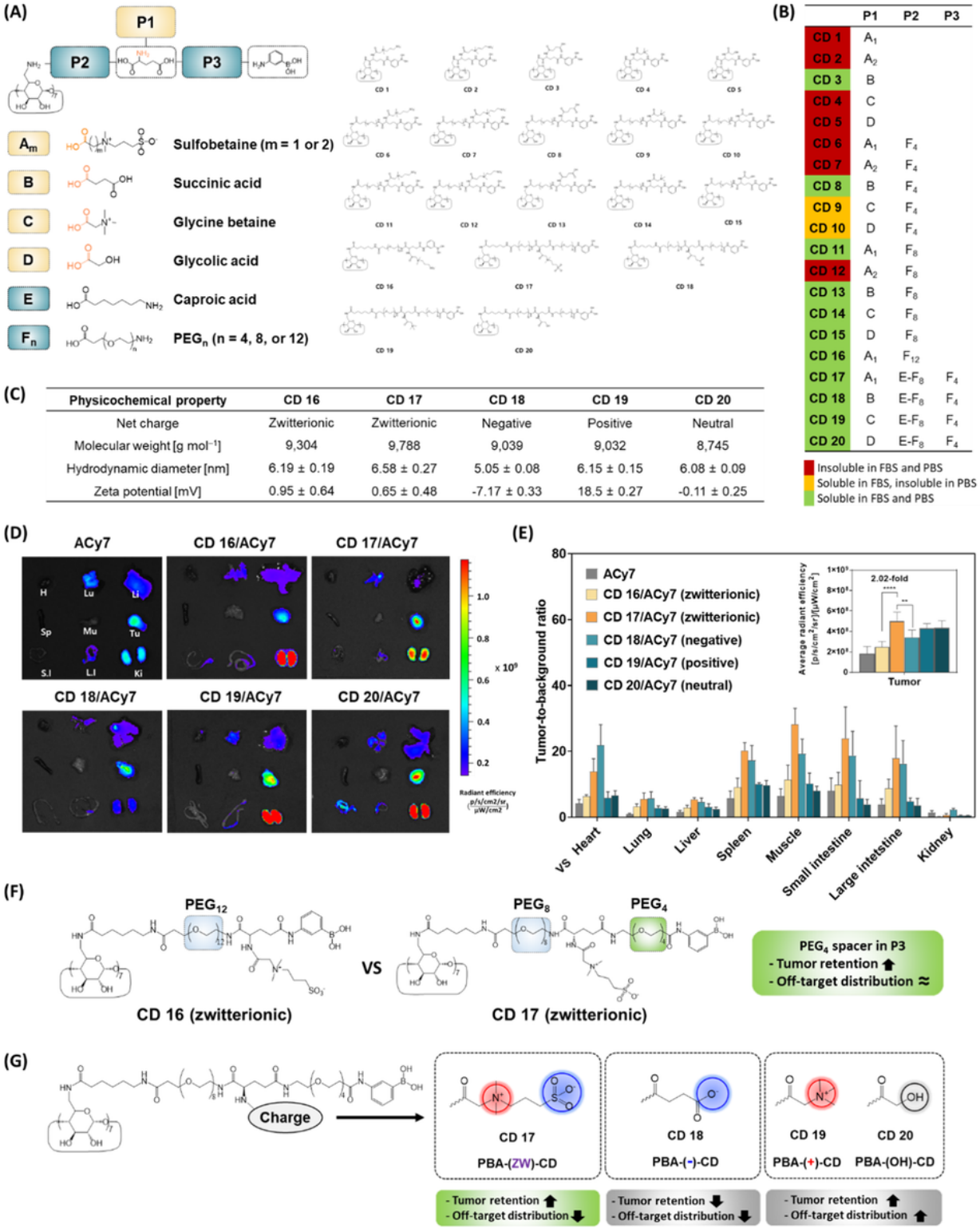

Figure 1

Renal clearable cyclodextrin (CD) derivatives for enhanced tumor retention and reduced off-target accumulation. (A) Schematic view of CD derivatization. The carboxylic acid of charged moieties (A_m, B, C, and D) was linked to the amine group of glutamic acid linker *via* amide bond formation (orange color) (P1). Various spacers (E and F_n) were introduced between CD ring and glutamic acid linker (P2) and glutamic acid and PBA moiety (P3). Magnified images of **CD 1–20** structures can be found in Supporting

Information. (B) Relationship between CD structure and colloidal stability. Turbidimetry-based solubility test was performed on CD derivatives dispersed in fetal bovine serum (FBS) or phosphate-buffered saline (PBS) at 1 mmol L^{-1} concentration. (C) Physicochemical properties of five candidate structures with high colloidal stability. (D) Biodistribution of **CD 16–20**/adamantyl sulfocyanine 7 (ACy7) inclusion complexes. *Ex vivo* near-infrared fluorescence (NIRF) images of tumors and major organs resected from HT-29 tumor-bearing mice 24 h after the intravenous injection of free ACy7 or inclusion complexes. Abbreviations: H, heart; Lu, lungs; Li, liver; Sp, spleen; Mu, muscle; Tu, tumor; S.I, small intestine; L.I, large intestine; and Ki, kidneys. (E) Tumor-to-background ratios of **CD 16–20**/ACy7 in each organ. Radiant efficiency values in tumor tissues are presented in the inset. (F) Addition of the PEG_4 spacer in the P3 position significantly improved the tumor accumulation of zwitterionic CD derivatives, presumably reducing the interference of sulfobetaine in PBA–target interactions. (F) Among four differently charged CD derivatives, only the zwitterionic CD derivative (**CD 17**, PBA-(ZW)-CD) exhibited enhanced tumor retention and reduced off-target accumulation simultaneously.

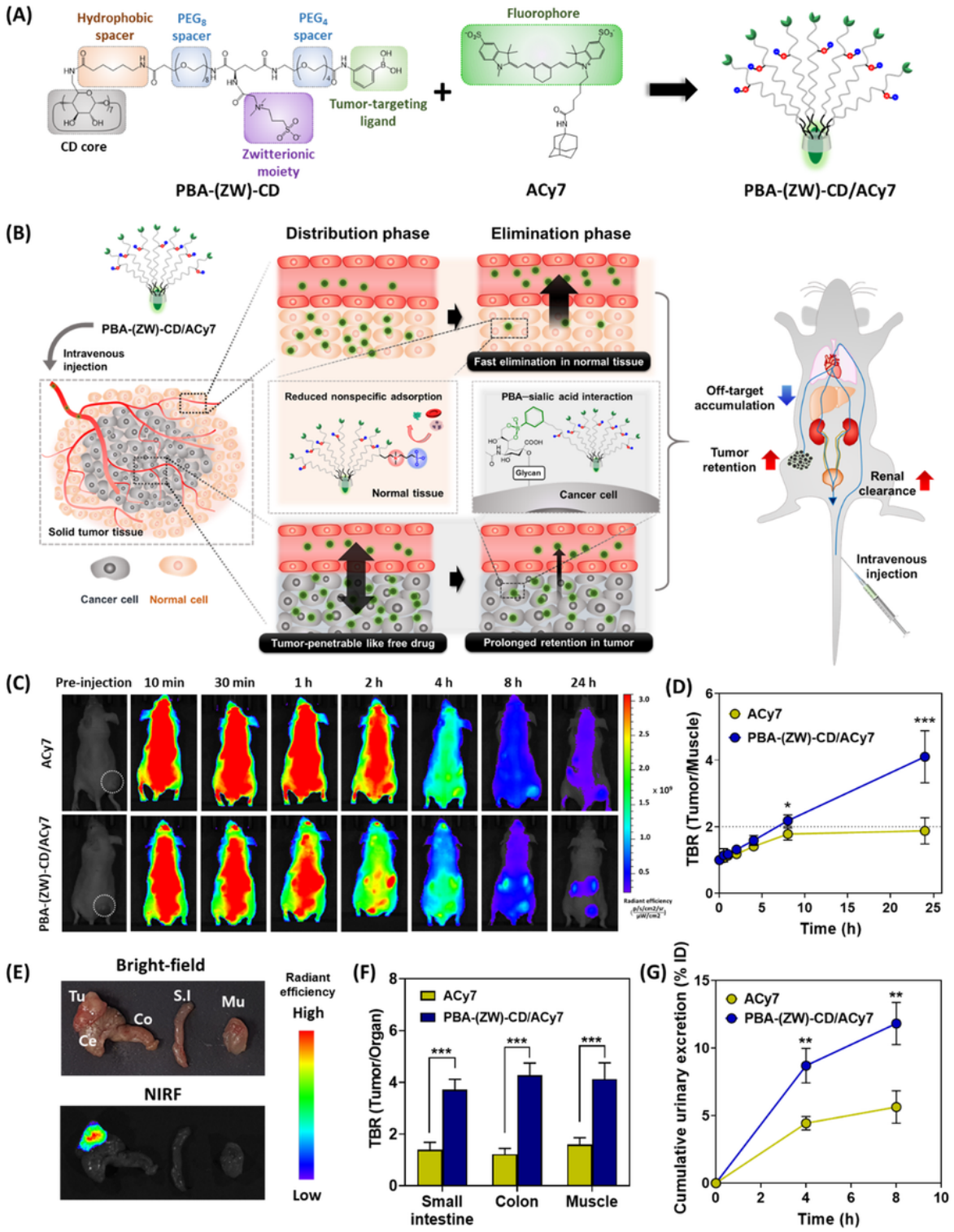

Figure 2

Tumor targetability, pharmacokinetics, and urinary excretion of PBA-(ZW)-CD/ACy7. (A) Structural components of PBA-(ZW)-CD/ACy7, including hydrophobic linker (caproic acid), PEG spacers, zwitterionic moiety (sulfobetaine), and tumor-targeting ligand (PBA). (B) Schematic illustration of the *in vivo* behavior of PBA-(ZW)-CD/ACy7 accounting for enhanced tumor retention and reduced off-target accumulation. (C) *In vivo* real-time NIRF imaging after intravenous administration of ACy7 or PBA-(ZW)-CD/ACy7 to

heterotopic (subcutaneous) HT-29 tumor-bearing mice (dashed circles indicate tumors) and (D) corresponding time-course changes in the tumor-to-background ratio (TBR). Data are presented as the mean ± standard deviation (SD) (n = 4). (E) *Ex vivo* NIRF images of HT-29 tumors (located at cecum [Ce] wall, colon [Co], small intestine [S.I], and muscle [Mu]), resected from orthotopic (subserosal) HT-29 tumor-xenografted mice 24 h after the intravenous injection of PBA-(ZW)-CD/ACy7. (F) TBR was measured in the colon, small intestine, and muscle tissues. Data are presented as the mean ± SD (n = 4). (G) Cumulative urinary excretion (% ID) of free ACy7 and PBA-(ZW)-CD/ACy7. Data are presented as the mean ± SD (n = 3). *p < 0.05, **p < 0.01, and ***p < 0.001.

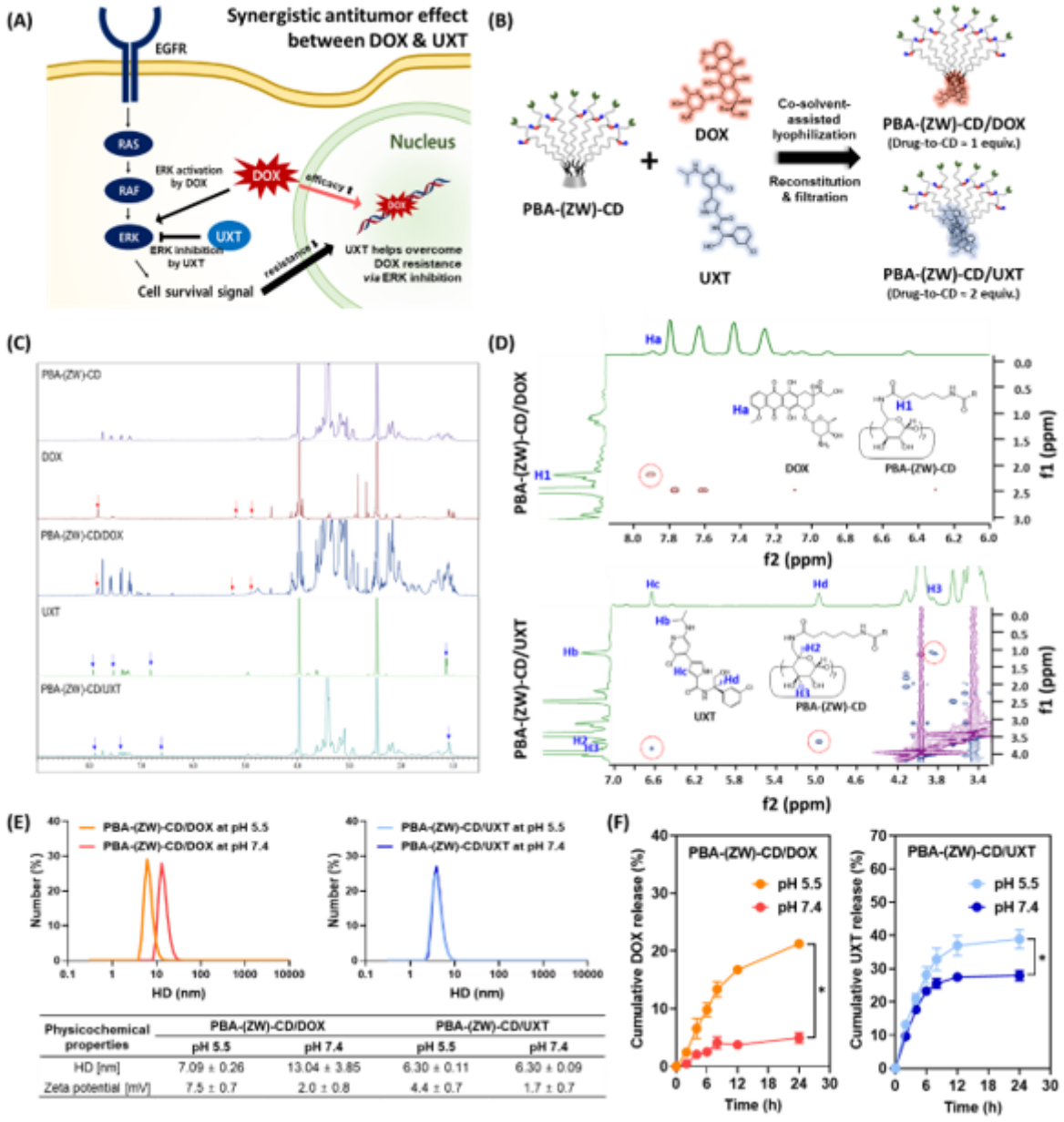

Physicochemical properties	PBA-(ZW)-CD/DOX		PBA-(ZW)-CD/UXT	
	pH 5.5	pH 7.4	pH 5.5	pH 7.4
HD [nm]	7.09 ± 0.26	13.04 ± 3.85	6.30 ± 0.11	6.30 ± 0.09
Zeta potential [mV]	7.5 ± 0.7	2.0 ± 0.8	4.4 ± 0.7	1.7 ± 0.7

Figure 3

Preparation and characterization of PBA-(ZW)-CD/drug inclusion complexes. (A) Schematic illustration of the synergistic antitumor efficacy of the doxorubicin (DOX) and ulixertinib (UXT) combination. UXT, a potent extracellular signal-regulated kinase (ERK) inhibitor, may counteract the DOX-induced ERK activation and consequent drug resistance. (B) Preparation of PBA-(ZW)-CD/DOX and PBA-(ZW)-CD/UXT inclusion complexes *via* lyophilization. (C) Proton nuclear magnetic resonance (^{1}H-NMR) spectra of free drugs and inclusion complexes. Slight changes in the chemical shifts of DOX (red arrows) and UXT (blue arrows) were observed after complexation. All samples were dissolved in dimethyl sulfoxide (DMSO)-d_6/D_2O (80:20, v/v). (D) ROESY spectra of PBA-(ZW)-CD/DOX and PBA-(ZW)-CD/UXT in DMSO-d_6/D_2O (80:20, v/v). Dashed circles indicate dipolar couplings supporting the inclusion complex formation. (E) Physicochemical properties, including number-weighted size distribution, mean hydrodynamic diameter (HD), and zeta potential, of inclusion complexes at pH 5.5 and 7.4. (F) Drug release profiles of PBA-(ZW)-CD/DOX and PBA-(ZW)-CD/UXT inclusion complexes at pH 5.5 and 7.4 (n = 3, *p < 0.005).

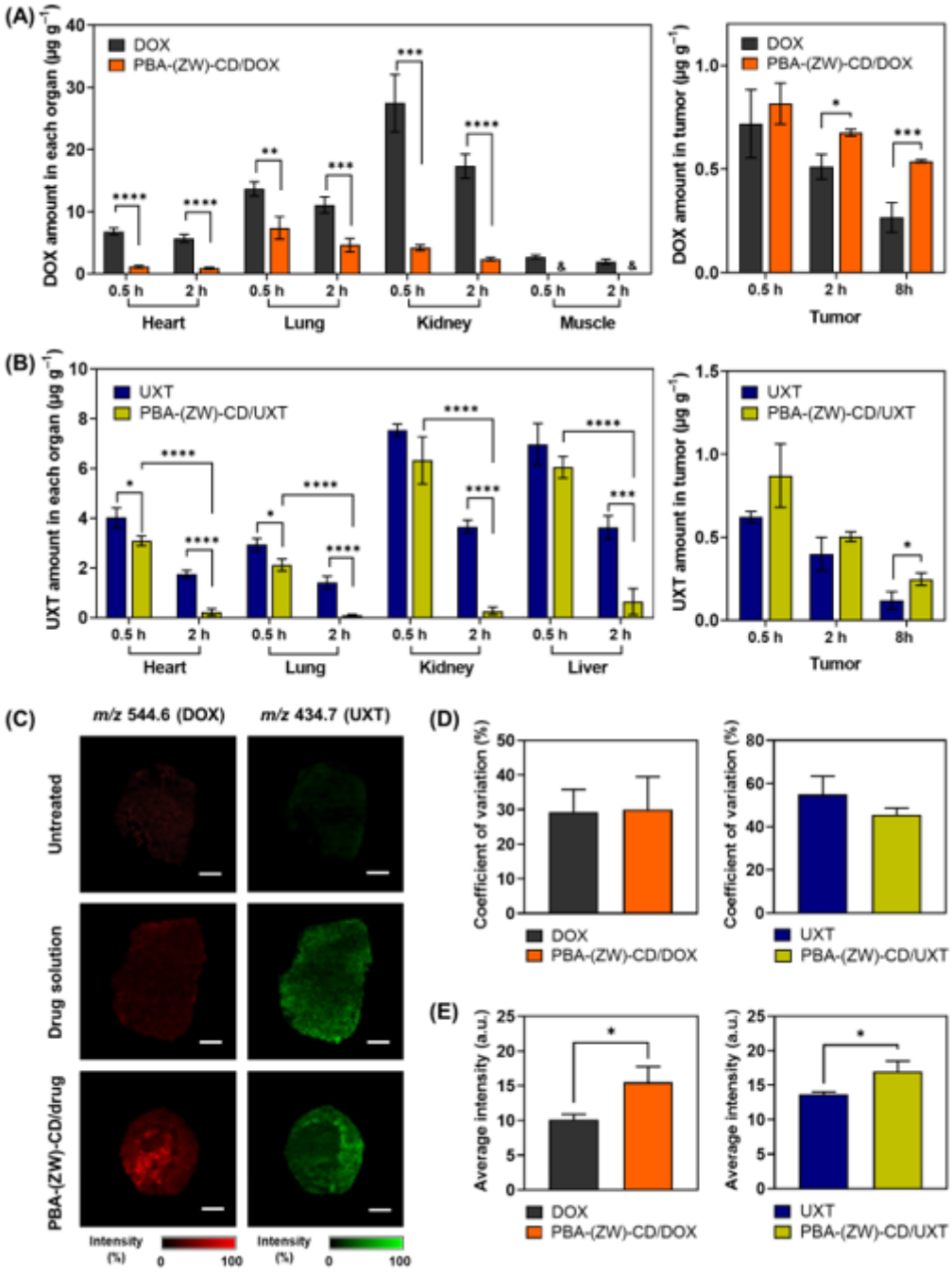

Figure 4

Biodistribution of PBA-(ZW)-CD/drug inclusion complexes. (A) DOX distribution in normal tissues related to drug adverse effects and tumor after the intravenous injection of DOX solution or PBA-(ZW)-CD/DOX at a DOX dose of 5 mg kg^{-1} (n = 3). (B) UXT distribution in normal tissues, including mononuclear phagocyte system (MPS)-rich organs, and tumor after the intravenous administration of UXT solution and PBA-(ZW)-CD/UXT at a UXT dose of 5 mg kg^{-1} (n = 3). (C) Matrix assisted laser desorption/ionization-mass spectrometry imaging (MALDI-MSI) study of tumor tissues dissected at 30 min post-injection of drug solution or PBA-(ZW)-CD/drug inclusion complex (n = 3). Intratumoral mass spectrometry (MS) signals corresponding to DOX (m/z 544.6, pseudocolored in red) and UXT (m/z 434.7,

pseudocolored in green) are presented. The length of scale bar is 1 mm. The spatial signal distributions as coefficient of variation (D) and area-averaged signal intensity (E) were also evaluated *via* image analysis. *$p < 0.05$, **$p < 0.01$, ***$p < 0.005$, and ****$p < 0.001$. [&] below the detection limit (< 200 ng g^{-1} tissue).

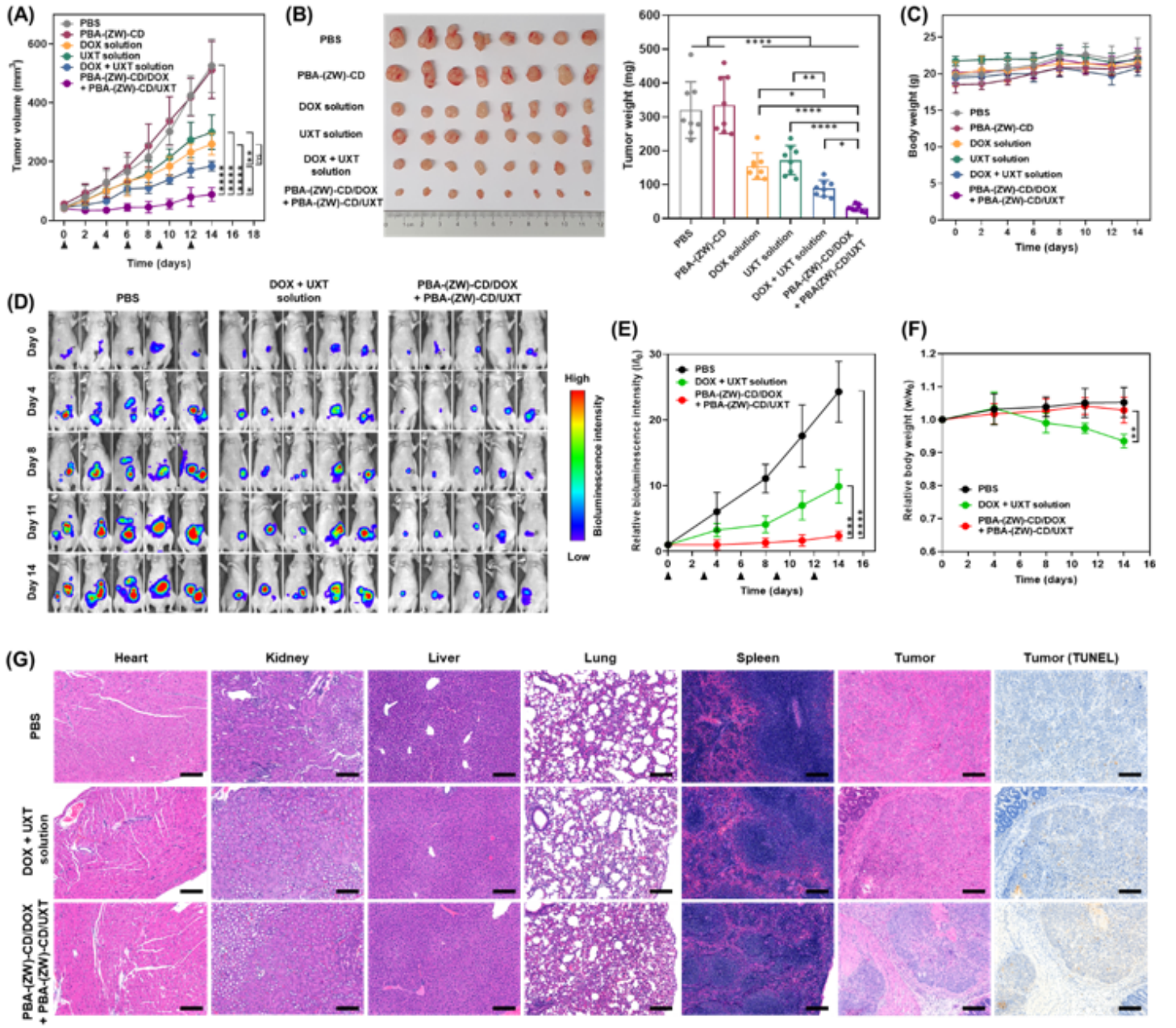

Figure 5

PBA-(ZW)-CD/drug-assisted combination therapy in colorectal cancer (CRC) models. (A) Tumor growth profile of heterotopic HT-29 xenograft mice treated with PBS, blank PBA-(ZW)-CD, DOX solution, UXT solution, DOX + UXT solution, or PBA-(ZW)-CD/DOX + PBA-(ZW)-CD/UXT (as drug, 3 mg kg^{-1} for each) intravenously every three days (n = 8). (B) On day 14, the tumor tissues were resected and weighed. (C) Body weight of each mouse was monitored during the experimental period. (D) *In vivo* bioluminescence

images of orthotopic CRC model prepared via the inoculation of HT-29/Luc cells into BALB/c nude mice (n = 5). (E) Relative bioluminescence intensity (I/I_0; compared to day 0) vs. time profile of PBS, DOX + UXT, and PBA-(ZW)-CD/DOX + PBA-(ZW)-CD/UXT groups. Mice were intravenously administered with each intervention (as drug, 3 mg kg^{-1} for each) every three days. (F) Body weight change of each mouse was recorded. (G) Hematoxylin and eosin (tumor and organs) and terminal deoxynucleotidyl transferase dUTP nick-end labeling (TUNEL; tumor) staining images of tissues dissected on day 14. The length of the scale bar is 200 μm. Data are presented as the mean ± SD. *p < 0.05, **p < 0.01, ***p < 0.005, and ****p < 0.001. ^{ns}p > 0.05, not significant.

Supplementary Files

This is a list of supplementary files associated with this preprint. Click to download.

- Supplementary.docx